RSC Advances

PAPER

View Article Online
View Journal | View Issue

Cite this: *RSC Adv.*, 2023, **13**, 8182

Ultralow diffusion barrier induced by intercalation in layered N-based cathode materials for sodium-ion batteries†

Yundan Jiang, Wangping Xu, Wei Zhao * and Juexian Cao*

Received 20th January 2023
Accepted 6th March 2023

DOI: 10.1039/d3ra00434a

rsc.li/rsc-advances

Sodium-ion batteries (SIBs) have attracted huge attention due to not only the similar electrochemical properties to Lithium-ion batteries (LIBs) but also the abundant natural reserves of sodium. However, the high diffusion barrier has hindered its application. In this work, we have theoretically studied the relationship between the strain and the diffusion barrier/path of sodium ions in layered CrN_2 by first-principles calculation. Our results show that the strain can not only effectively decrease the diffusion barrier but also change the sodium diffusion path, which can be realized by alkali metal intercalation. Moreover, the diffusion barrier is as low as 0.04 eV with the Cs atoms embedding in layered CrN_2 ($Cs_{1/16}CrN_2$), suggesting an excellent candidate cathode for SIBs. In addition, the decrease of the barrier mainly originated from the fact that interlayer electronic coupling weakened with the increase of interlayer spacing. Our findings provide an effective way to enhance sodium diffusion performance, which is beneficial for the design of SIB electrode materials.

1. Introduction

Lithium-ion batteries (LIBs) have attracted much attention for their wide application in energy storage over the past decades.[1,2] However, the uneven distribution and limited reserves of lithium resources hinder their application.[3] In contrast, sodium-ion batteries (SIBs) not only have similar properties to LIBs but also have the advantages of abundant reserves, low cost and being environment-friendly.[4,5] The cathode material plays a critical role in battery performance, and the ideal cathode materials are supposed to possess a high capacity and low diffusion barrier.[6,7] Therefore, screening new cathode materials with excellent electrochemical performance is an effective way to facilitate the development and application of SIBs.

Conventional SIBs cathodes have promoted the development of sodium-ion batteries to a certain extent, including transition metal oxides,[8] polyanionic compounds[9] and Prussian blue analogs,[10] but the low capacity and high diffusion barrier greatly hinder SIBs application. Recently, layered materials have received much attention due to their unique geometry structures for SIBs, including layered transition oxides, transition metal dichalcogenides (TMDs), and other two-dimensional layered materials.[11–15] Transition metal oxides possess high specific capacities and free pollution, while the poor structural stability during the process of charging and discharging limits their application.[16] TMDs also have a high theoretical capacity and structural stability because of their unique sandwich structures, while the lower conductivity and volume expansion will result in poor rate capability and cycle stability.[12,17] Furthermore, two-dimensional monolayer materials, such as ScO_2, BP_2 and V_2O_5, boast large surface areas, which provide a wide range of sodium storage sites, but they also exhibit poor electrical conductivity.[18–20] It is worth noticing that two-dimensional transition metal N-based materials (*i.e.* MoN_2, VN_2 and Zr_2N) have both high capacity and excellent electronic conductivity, suggesting that they can serve as potential cathode SIBs materials.[21–23] In particular, layered CrN_2 has been proven to be a promising candidate for sodium-ion batteries for its high theoretical capacity and high voltage platform.[24] However, due to the strong interlayer coupling, the diffusion barrier of layered CrN_2 is still too high for practical application. Therefore, it is urgent to explore an efficient way to improve the diffusion performance of SIBs.

Strain engineering, which can be realized by element intercalating and mechanical loading, is a simple and efficient way to lower the Na-ion diffusion barrier and improve the

Department of Physics & Hunan Institute of Advanced Sensing and Information Technology, Xiangtan University, Xiangtan 411105, PR China. E-mail: zhaowei@xtu.edu.cn; jxcao@xtu.edu.cn

† Electronic supplementary information (ESI) available: The details of setting the magnetic order and the *U* value were put in ESI. Fig. S1 shows the four magnetic orders of the calculated system. Fig. S2 is a linear fit of the number of d-electrons on Cr as a function of the additional potential φ. The results of phonon spectrum and AIMD calculations are shown in Fig. S3. The relationship between the diffusion barrier and *c*-axis strain along two different diffusion paths were shown in Fig. S4. Fig. S5 gives the energy profile of sodium ions along the diffusion path in CrN_2 without intercalation. Fig. S6 shows the most stable configuration of $Na_xCs_{1/16}CrN_2$ (x = 0–1) under different sodium concentrations. Fig. S7 shows the projected band (PBAND) and projected density of states (PDOS) for N in $ACrN_2$ (A = Na, K, Rb and Cs). See DOI: https://doi.org/10.1039/d3ra00434a

conductivity properties for designing electrode materials of SIBs.[25,26] Thus, in this work, we have theoretically studied the relationship between the strain and the diffusion barrier/path of sodium ions in layered CrN_2 by first-principles calculation, which can be realized by alkali metal intercalation. The results show that the strain can not only effectively decrease the diffusion barrier but also change the sodium diffusion path. Furthermore, the diffusion barrier is low as 0.04 eV with the Cs atoms embedding in layered CrN_2 ($Cs_{1/16}CrN_2$), implying a fascinating candidate cathode material for SIBs. Besides, the decrease in the barrier mainly originated from the fact that interlayer electronic coupling weakened with the increase of interlayer spacing.

2. Computational details and models

All of the calculations were performed using the Vienna *ab initio* simulation package (VASP) based on the density functional theory (DFT).[27,28] The exchange–correlation interaction between electrons was described by Perdew–Burke–Ernzerhof (PBE) functional in Generalized Gradient Approximation (GGA) theory with Hubbard U correction for the self-interaction errors.[29,30] The value of U for Cr (3.69 eV) was determined according to the linear response method which was discussed in detail in ESI.†[31] The cutoff energy for expanding plane wave function was set to 450 eV. The criterion of energy and force convergence was set to 10^{-6} eV and 0.01 eV $Å^{-1}$, respectively. The *k*-points for structural relaxation were set to be 12 × 12 × 3. The van der Waals interactions (DFT-D3) were considered in all calculations to correct the long–range interactions between interlayers.[32]

To discuss the intercalation and diffusion performance of sodium ions in CrN_2, a 4 × 4 × 1 supercell consisting of 32 Cr atoms and 64-N atoms was used, and a 3 × 3 × 3 K-point grid was adopted. The Climbing Image Nudge Elastic Band (CI-NEB) method was used to calculate the Na diffusion performance.[33]

The intercalation energy E_{inter} of Na intercalating in the interlayer is defined as eqn (1):

$$E_{inter} = (E_{Na_xX} - E_X - x\mu_{Na})/x \quad (1)$$

Here, E_{Na_xX} represents the total energy of the X cathode that intercalated *x* Na atoms; E_X is the total energy of the X cathode; μ_{Na} is the chemical potential of Na atom.

The theoretical capacity[34] *C* is defined according to formula (2):

$$C = \frac{nF}{3.6M} \quad (2)$$

Here, *n* is the valence electron number of sodium ($n = 1$), *F* is the Faraday constant ($F = 96\,485$ C mol^{-1}), and *M* is the relative molecular weight in the molecular formula.

The voltage[35] *V* is calculated by the formula (3):

$$V = -\left(E_{Na_{x_2}X} - E_{Na_{x_1}X} - (x_2 - x_1)\mu_{Na}\right)\Big/(x_2 - x_1)e \quad (3)$$

Here, $E_{Na_{x_2}X}$ and $E_{Na_{x_1}X}$ are the total energy of E_{Na_xX} at concentrations of x_1 and x_2, respectively. μ_{Na} is the chemical potential of the Na atom, and *e* is the electric quantity of an electron ($e = 1.6 \times 10^{-19}$ C). In all of the above formulas, X refers to $Cs_{1/16}CrN_2$.

The two sandwich-like structure models of CrN_2, which are highly similar to TMDs, were studied in this work, as shown in Fig. 1. Among them, each Cr forms different coordination structures with six N, which are divided into 2H-phase (octahedral coordination structure with AB stacking order of CrN_2 layers) and 1T-phase (triangular prismatic coordination structure with AA stacking order of CrN_2 layers) according to the coordination structure formed by Cr and N and the stacking order of CrN_2 layers. The single cells of the 2H-phase and 1T-phase are all hexagonal cells. In the 2H-phase, a unit cell contains 2-layers of CrN_2, including 2-Cr atoms and 4-N atoms. In the 1T-phase, a unit cell contains 1 CrN_2 layer, including 1-Cr atom and 2-N atoms. Therefore, a 1 × 1 × 1 unit-cell of 2H-phase and 1 × 1 × 2 supercell of 1T-phase were used for calculations, both of which have 2 CrN_2 layers containing 2-Cr atoms and 4-N atoms. The lattice constants of the calculated 2H-phase CrN_2 are $a = b = 3.20$ Å and $c = 7.90$ Å, and those of the calculated 1T-phase are $a = b = 2.78$ Å and $c = 8.66$ Å. Similar to conventional TMDs, the formation energy of the 2H-phase is lower than that of the 1T-phase, indicating that 2H enjoys better structural stability.[36] Besides, as shown in Fig. S3,† 2H–CrN_2 has both good kinetic and thermodynamic stability according to phonon spectra and *ab initio* molecular dynamics (AIMD) calculations. Moreover, the 2H-phase CrN_2 has the advantages of high theoretical capacity and high electrode potential, which makes it have considerable potential to be applied in the cathode materials of sodium-ion batteries.[24]

3. Results and discussions

3.1 Strain effect of CrN_2

To improve the diffusion performance of CrN_2, we established a toy model to study the regulation of strain on its diffusion performance. In this model, 0–20% tensile strain is applied to the *c*-axis, and all Cr and N atoms are fixed to ensure that the *c*-axis strain can be maintained after the structure is fully relaxed. Among them, the most stable intercalation site of sodium is the octahedral gap between the CrN_2 layers (position O in Fig. 2a and b). The possible diffusion path is that Na diffuses along the top side of the Cr atom (O–T–O) or the bridge site of the Cr–N bond (O–B–O) between two adjacent insertion sites, respectively. The results show that the diffusion barrier decreases significantly with the increase of strain, as is shown in Fig. 2c. At low strain, Na tends to diffuse along the path of O–T–O; when the strain increases to more than 16%, the diffusion barriers of the two diffusion paths are almost equal, indicating that Na will diffuse along the two paths at the same time, as is shown in Fig. S4.† The change in diffusion barrier and path is mainly induced by the increase of interlayer spacing, as is shown in Fig. 2c.

In experiments, interlayer spacing can usually be increased by large ion intercalating. In order to maintain the charge balance of the system, alkali and alkaline earth metals with similar electronegativity to sodium were selected as intercalated ions. Since both alkali metals and alkaline earth metals (Ca, Sr,

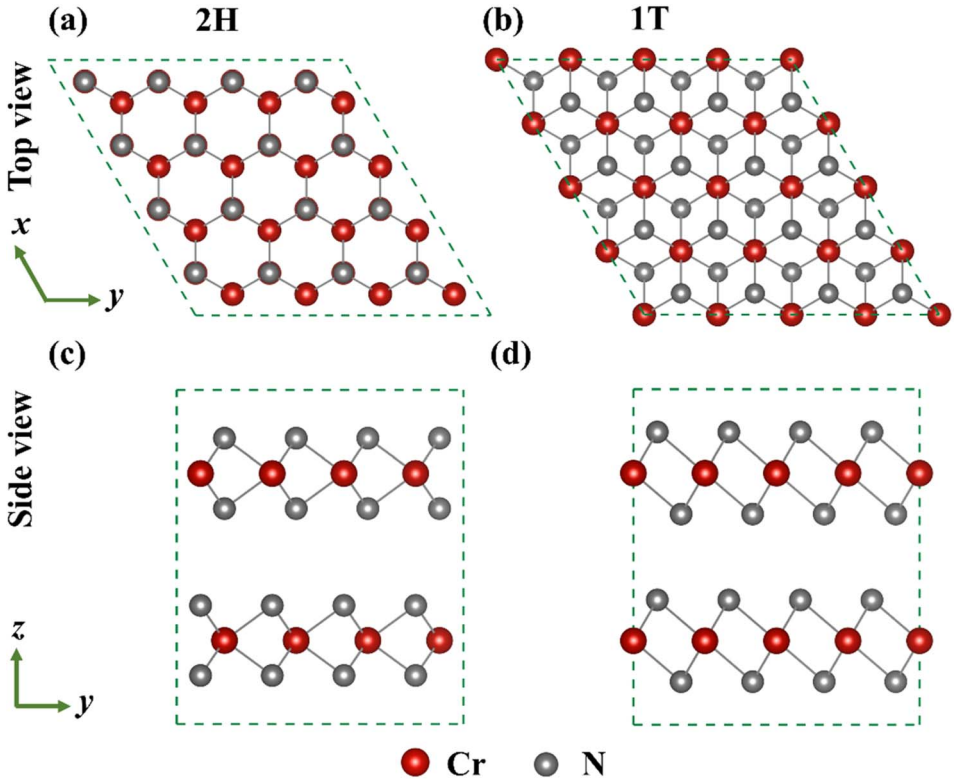

Fig. 1 The top and side views of 2H-phase (a) (c) and 1T-phase (b) (d) CrN_2 structure, respectively (Dark red sphere and gray sphere represent Cr and N atoms, respectively.).

Ba, K, Rb and Cs) have larger ionic radius than Na (except Ca), their embedding between CrN_2 layers will increase the interlayer spacing so that CrN_2 can obtain a larger strain in the *c*-axis direction. Its intercalated structure is shown in Fig. 3a and b, and the intercalated concentration is 6.25%. The interlayer spacing of CrN_2 increases with the increase of the intercalated atomic radius of the interlayer, as is shown in Fig. 3c. The increase in interlayer spacing will lead to the increase of the *c*-

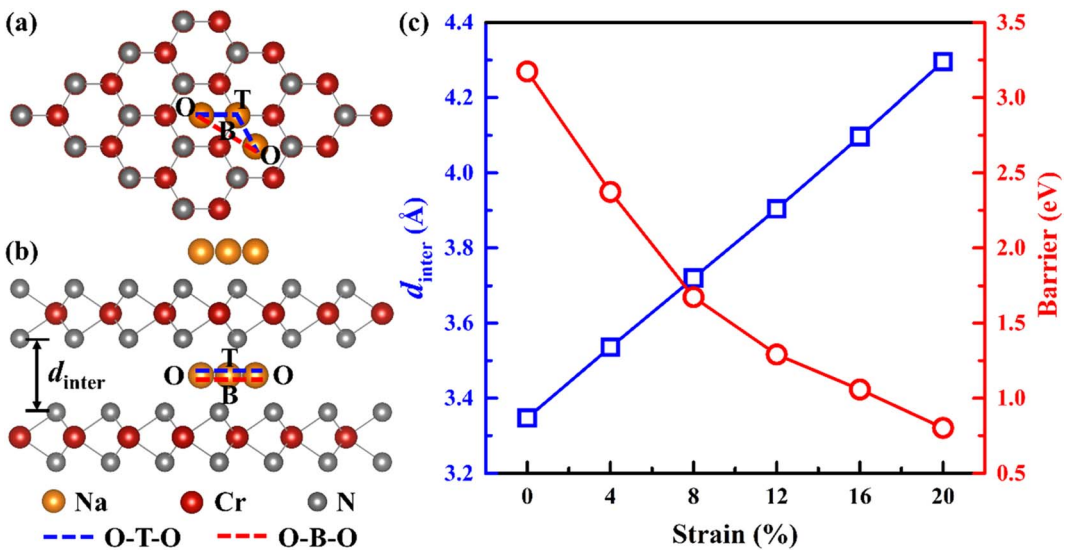

Fig. 2 The diffusion path of Na in CrN_2 (O–T–O or O–B–O) and the most stable intercalation site (O) of Na (a) top view (b) side view and the interlayer spacing (d_{inter}) of CrN_2 (orange sphere, dark red sphere and gray sphere represent Na, Cr and N atoms, respectively. The blue and red dashed lines represent diffusion paths along O–T–O or O–B–O, respectively); (c) the relationship between interlayer spacing and diffusion barrier with strain.

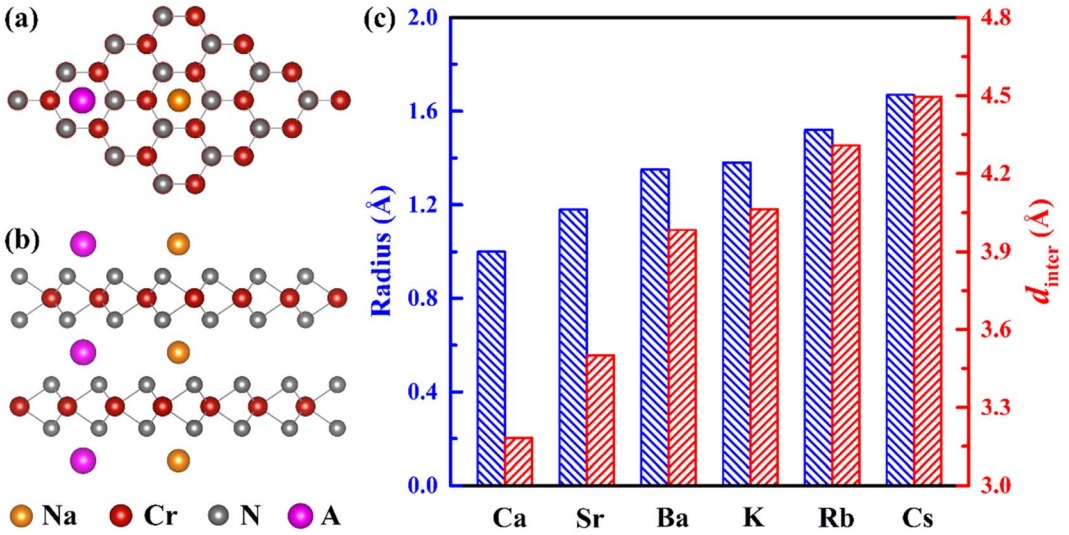

Fig. 3 Structure of alkali or alkaline earth metal intercalated in CrN_2 (a) top view (b) side view (orange, dark red, and gray spheres represent Na, Cr, and N, respectively, and purple spheres represent alkali or alkaline earth metals containing K, Rb, Cs, Ca, Sr and Ba); (c) atomic radius of the alkali metal or alkaline earth metal and the interlayer spacing of CrN_2 after intercalation.

axis, thus realizing the tensile strain of the *c*-axis. Among them, the Cs atom has the largest ionic radius (1.67 Å), and the CrN_2 interlayer spacing reaches 4.5 Å after Cs intercalation, which is much larger than that of CrN_2 without intercalation (3.35 Å). A larger layer spacing will be conducive to the diffusion of Na between interlayers, making it easier to intercalate and de-intercalate Na, thus improving the rate capability of the material. In addition, in the process of battery charging and

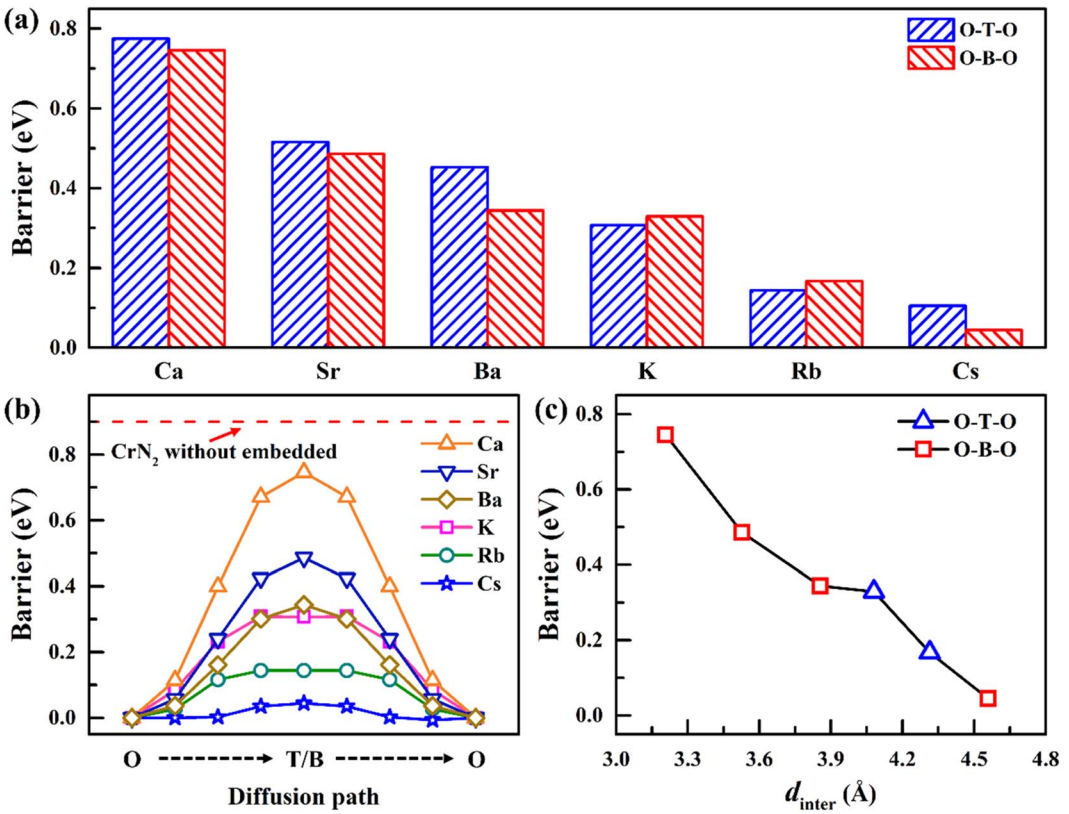

Fig. 4 (a) Diffusion barrier of Na along O–T–O or O–B–O paths in $A_{1/16}CrN_2$ (A = K, Rb, Cs, Ca, Sr and Ba); (b) diffusion energy profile of Na along the lowest barrier path in $A_{1/16}CrN_2$ (A = K, Rb, Cs, Ca, Sr and Ba) (red dashed line represents the barrier of Na in CrN_2 without atoms embedded, and Fig. S5† shows its diffusion energy profile); (c) the relationship between diffusion barrier and diffusion path with interlayer spacing.

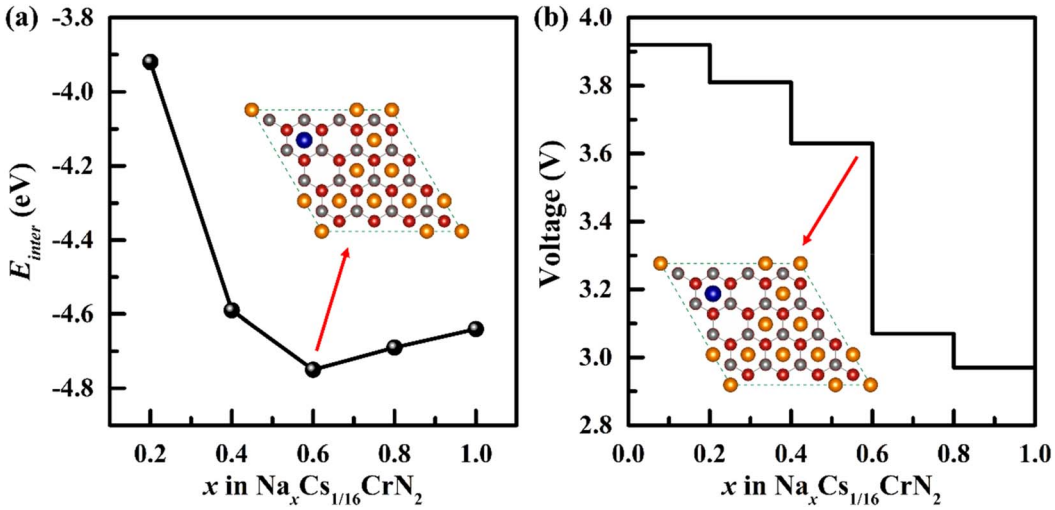

Fig. 5 (a) The intercalation energy (E_{inter}) of Na in $Cs_{1/16}CrN_2$ at various concentrations. (b) The voltage profile of Na embedded in $Cs_{1/16}CrN_2$ (the illustration shows the intercalation structure with a Na concentration of 0.6, and the most stable intercalation structure at each concentration is shown in Fig. S6†).

discharging, the interlayer atoms can better maintain the structural stability of CrN_2, reduce the collapse of CrN_2 in the case of complete Na removal, and improve the cyclic stability of the material.

To further study the influence of alkali metal or alkaline earth metal intercalation on the diffusion barrier of Na, we calculated the diffusion barrier of Na along the O–T–O or O–B–O path, respectively. The results show that the diffusion barrier of

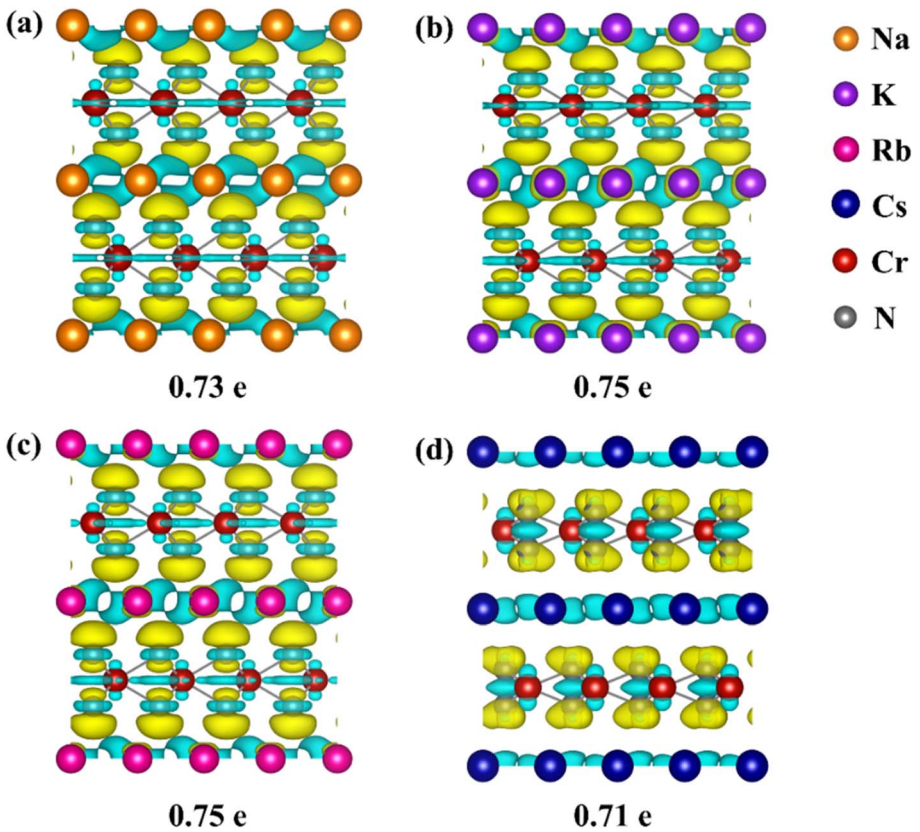

Fig. 6 Differential charge density and charge transfer for CrN_2 with Na (a) K (b) Rb (c) Cs (d) intercalation (orange, purple, rose, dark blue, dark red, and gray spheres represent Na, K, Rb, Cs, Cr, and N atoms, respectively. Yellow areas and light blue areas represent electron-rich regions and electron-deficient regions, respectively. The isosurface level is set to 0.003 e $Å^{-3}$).

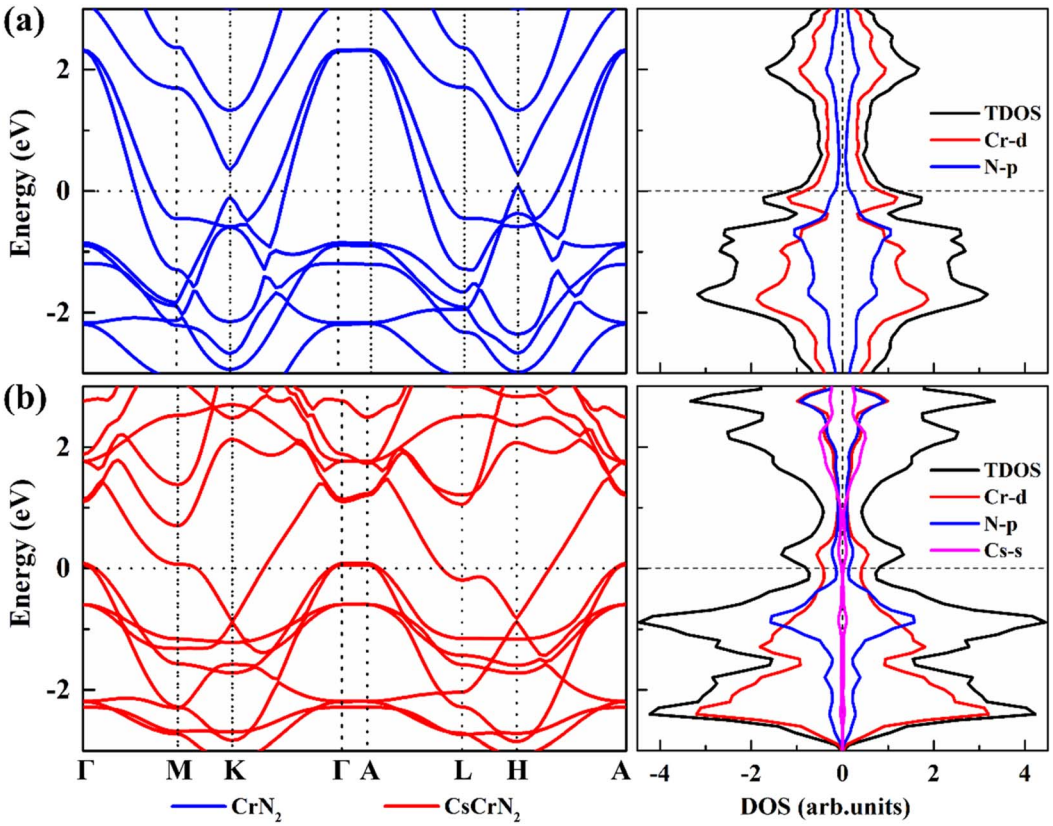

Fig. 7 Band structure and density of states of (a) CrN_2 and (b) $CsCrN_2$. The Fermi level is set to 0.

Na decreases significantly with the increase of the intercalated atomic radius, as is shown in Fig. 4a and b. Especially after Cs intercalation, the diffusion barrier of Na decreases to 0.04 eV, which is significantly lower than that of CrN_2 without intercalation (0.9 eV). The change in diffusion barrier is mainly caused by the increases in interlayer spacing after ion intercalation. With the increase of interlayer spacing, the diffusion barrier decreases sharply, as is shown in Fig. 4c. Furthermore, the diffusion path has changed with the different intercalation elements. Specifically, Na diffuses through the O–T–O path for CrN_2 for K and Rb intercalation, while for Cs intercalation, it through the O–B–O path for CrN_2, as is shown in Fig. 4a and c. But for alkaline earth metals (Ca, Sr and Ba) intercalation, the diffusion only follows the O–B–O path due to the large quantity of charge (high valence state), as is shown in Fig. 4a and c. Besides, the volume change rate of $Cs_{1/16}CrN_2$ during the sodium diffusion process is only 3% due to the structural stabilization effect of Cs ion embedding.

3.2 Properties of $Cs_{1/16}CrN_2$

The intercalation energy of Na ions in $Cs_{1/16}CrN_2$ is a key parameter to measure the difficulty of intercalation. Therefore, we calculated the intercalation energy of Na ions in $Cs_{1/16}CrN_2$ at different concentrations. Fig. S6† shows the most stable structure of Na intercalation at different concentrations. The calculated intercalation energy at different concentrations is shown in Fig. 5a. The results show that at low concentrations (less than 0.6), the intercalation energy decreases with the increase of Na concentration because the effective interaction of sodium ions is attractive. However, when the concentration of Na goes beyond 0.6, the effective interaction of sodium ions becomes repulsive, and the intercalation energy increases with Na concentrations; as is shown in Fig. 5a. Overall, the negative intercalation energy allows Na to be embedded easily in $Cs_{1/16}CrN_2$. Moreover, $Cs_{1/16}CrN_2$ has larger negative intercalation energy than CrN_2 without Cs intercalating, indicating that Na can intercalate in $Cs_{1/16}CrN_2$ more easily.[24]

Electrode potential is another important parameter of electrode materials. We calculated the voltage of $Cs_{1/16}CrN_2$ at different Na concentrations. The results show that $Na_xCs_{1/16}CrN_2$ has a high voltage platform of 3.0–3.9 V, as is shown in Fig. 5b. According to the voltage calculation formula, when $x_1 = 0$, $x_2 = 1$, the calculated voltage (3.5 V) is the open circuit voltage. Such high voltage makes it have high output power as the cathode for SIBs. Furthermore, the initial voltage (3.9 V) and average voltage (3.5 V) of CrN_2 with Cs intercalating are both higher than that of CrN_2 without Cs intercalating (initial voltage of 3.8 V and average voltage of 3.4 V).[24]

Theoretical capacity, another important parameter of electrode materials, determines the energy density of electrode materials. The theoretical capacity of $Cs_{1/16}CrN_2$ is calculated to be 285 mA h g^{-1}. The energy density D was calculated according to $D = C \cdot V$, here C and V represents the theoretical capacity and open circuit voltage, respectively.[37] Thus the calculated energy

density of $Cs_{1/16}CrN_2$ is 903 W h kg^{-1}, higher than traditional transition metal oxides (less than 800 W h kg^{-1}), polyanions (less than 500 W h kg^{-1}) and Prussian blue compounds (about 500 W h kg^{-1}).[38]

To reveal the mechanism of the effect of alkali metal intercalation on diffusion properties, we studied the charge transfer for CrN_2 with alkali metal intercalation. Differential charge density and Bader charge analysis are used to visualize and measure charge transfer, respectively. Fig. 6 shows the differential charge density and charge transfer. The yellow electron-rich regions within the CrN_2 layer and the light blue electron-poor regions between the layers indicate that electrons are transferred from the intercalated atoms to CrN_2. For all alkali metals, the number of lost electrons is almost equal (about 0.71–0.75 *e*), indicating that the amount of charge transfer has little effect on the diffusion barrier. Furthermore, the coupling pattern changes because of increasing interlayer spacing with a radius of intercalated atoms increasing. Moreover, we have calculated the band structure of $ACrN_2$ (A = Na, K, Rb and Cs) projected onto N with different orbital symmetries and the projected density of states for N atoms, as shown in Fig. S7.† For CrN_2 with Na, K and Rb intercalation, the electrons transfer from s orbital of alkali metal atoms to out-of-plane p_z orbital of N atoms, which shows interlayer coupling. In contrast, For CrN_2 with Cs intercalation, the electrons transfer from s orbital of Cs atoms to in-plane $p_{x/y}$ orbital of N atoms, which shows intralayer coupling. Therefore, there is a strong coupling between the alkali metal and N atoms for Na, K and Rb intercalation but a weak coupling for Cs intercalation. This result is coincident with the foregoing analysis of differential charge density. Therefore, the distinct decreases of diffusion barrier are mainly induced by the transition from interlayer coupling to intralayer coupling.

To further investigate the effect of Cs intercalation on the electronic properties of CrN_2, we calculated the band structure and density of states of CrN_2 before intercalation and after Cs intercalation, respectively, as shown in Fig. 7. In band structure, it is shown that both CrN_2 and $CsCrN_2$ exhibit metallicity, which endows them with a fast charge and discharge rate. According to the total density of states near the Fermi level, both of them are antiferromagnetic. Moreover, the density of states far from the Fermi level in the conductive band moves close to the Fermi level after Cs embeds, which increases the carrier concentration. Charge carriers of higher concentrations enhance the conductivity and further improve the charge and discharge rate so that the CrN_2 with Cs embedded exhibits excellent rate performance.

4. Conclusions

In conclusion, based on the first-principles calculation, we have theoretically studied the relationship between the strain and the diffusion barrier/path of sodium ions in layered CrN_2. Our results show that all of $A_{1/16}CrN_2$ (A = Ca, Sr, Ba, K, Rb, and Cs) generate a large strain that causes a large interlayer spacing of over 3.2 Å arising from the large ionic radius of alkaline earth metal and alkali metal embedding. In particular, $Cs_{1/16}CrN_2$ takes on a 4.5 Å interlayer spacing, thus it boasts an extremely low barrier of 0.04 eV. Moreover, the Na diffusion path changes with the increase of interlayer spacing. Importantly, the decrease of the barrier is primarily due to the transition from the interlayer to intralayer electronic coupling with the increasing interlayer spacing. Finally, the high theoretical capacity (285 mA h g^{-1}) and the high voltage platform (3.0–3.9 V) of $Cs_{1/16}CrN_2$ reveal it as an excellent cathode material for SIBs. Above all, Cs intercalating not only makes CrN_2 obtain an ultra-low barrier but also improves its electrochemical performance. Our research provides a very effective approach to designing cathode materials with excellent performance for SIBs.

Conflicts of interest

There are no conflicts of interest to declare.

Acknowledgements

This work is supported by the National Natural Science Foundation of China (No. 11604278, 52073243, 12204398). National Key Research and Development Program of China (2020YFA0714703). The science and technology innovation Program of Hunan Province (2020RC1009, 2022RC3027). Xiangtan Science and Technology Bureau (ZD-ZD20211002).

Notes and references

1 M. Li, J. Lu, Z. Chen and K. Amine, *Adv. Mater.*, 2018, **30**, 1800561.
2 D. Di Lecce, R. Verrelli and J. Hassoun, *Green Chem.*, 2017, **19**, 3442–3467.
3 K. Chayambuka, G. Mulder, D. L. Danilov and P. H. L. Notten, *Adv. Energy Mater.*, 2020, **10**, 2001310.
4 D. Kundu, E. Talaie, V. Duffort and L. F. Nazar, *Angew. Chem., Int. Ed. Engl.*, 2015, **54**, 3431–3448.
5 C. Vaalma, D. Buchholz, M. Weil and S. Passerini, *Nat. Rev. Mater.*, 2018, **3**, 18013.
6 Z. Dai, U. Mani, H. T. Tan and Q. Yan, *Small Methods*, 2017, **1**, 1700098.
7 Z.-X. Huang, Z.-Y. Gu, Y.-L. Heng, E. Huixiang Ang, H.-B. Geng and X.-L. Wu, *Chem. Eng. J.*, 2023, **452**, 139438.
8 K. Kubota, S. Kumakura, Y. Yoda, K. Kuroki and S. Komaba, *Adv. Energy Mater.*, 2018, **8**, 1703415.
9 L. Xiao, F. Ji, J. Zhang, X. Chen and Y. Fang, *Small*, 2023, **19**, e2205732.
10 Q. Liu, Z. Hu, M. Chen, C. Zou, H. Jin, S. Wang, S. L. Chou, Y. Liu and S. X. Dou, *Adv. Funct. Mater.*, 2020, **30**, 1909530.
11 F. Wei, Q. Zhang, P. Zhang, W. Tian, K. Dai, L. Zhang, J. Mao and G. Shao, *J. Electrochem. Soc.*, 2021, **168**, 050524.
12 P. Ge, L. Zhang, Y. Yang, W. Sun, Y. Hu and X. Ji, *Adv. Mater. Interfaces*, 2019, **7**, 1901651.
13 E. Yang, H. Ji and Y. Jung, *J. Phys. Chem. C*, 2015, **119**, 26374–26380.
14 L. Shi and T. Zhao, *J. Mater. Chem. A*, 2017, **5**, 3735–3758.

15 A. Ghosh, S. Pal and P. Sarkar, *J. Phys. Chem. C*, 2022, **126**, 5092–5100.
16 P.-F. Wang, Y. You, Y.-X. Yin and Y.-G. Guo, *Adv. Energy Mater.*, 2018, **8**, 1701912.
17 M. Feng, M. Zhang, H. Zhang, X. Liu and H. Feng, *Carbon*, 2019, **153**, 217–224.
18 Z. Liu, H. Deng, S. Zhang, W. Hu and F. Gao, *J. Mater. Chem. A*, 2018, **6**, 3171–3180.
19 X. J. Ye, J. Xu, Y. D. Guo and C. S. Liu, *Phys. Chem. Chem. Phys.*, 2021, **23**, 4386–4393.
20 J. Zeng, J. Huang, J. Liu, T. Xie, C. Peng, Y. Lu, P. Lu, R. Zhang and J. Min, *Carbon*, 2019, **154**, 24–32.
21 X. Zhang, Z. Yu, S.-S. Wang, S. Guan, H. Y. Yang, Y. Yao and S. A. Yang, *J. Mater. Chem. A*, 2016, **4**, 15224–15231.
22 J. Xu, D. Wang, Y. Liu, R. Lian, X. Gao, G. Chen and Y. Wei, *J. Mater. Chem. A*, 2019, **7**, 26858–26866.
23 G. Liu, S. Xu, L. Wu, J. Zhang, Q. Wang and P. Lu, *Mater. Chem. Phys.*, 2020, **250**, 123028.
24 Y. Jiang, W. Xu, W. Zhao and J. Cao, *RSC Adv.*, 2022, **12**, 34200–34207.
25 P. Xiong, F. Zhang, X. Zhang, S. Wang, H. Liu, B. Sun, J. Zhang, Y. Sun, R. Ma, Y. Bando, C. Zhou, Z. Liu, T. Sasaki and G. Wang, *Nat. Commun.*, 2020, **11**, 3297.
26 C. Zhang, R. Gao, L. Zheng, Y. Hao and X. Liu, *ACS Appl. Mater. Interfaces*, 2018, **10**, 10819–10827.
27 G. Kresse and J. Furthmuller, *Phys. Rev. B: Condens. Matter Mater. Phys.*, 1996, **54**, 11169–11186.
28 G. Kresse and D. Joubert, *Phys. Rev. B: Condens. Matter Mater. Phys.*, 1999, **59**, 1758–1775.
29 J. P. Perdew, K. Burke and M. Ernzerhof, *Phys. Rev. Lett.*, 1996, **77**, 3865–3868.
30 H. J. Kulik, M. Cococcioni, D. A. Scherlis and N. Marzari, *Phys. Rev. Lett.*, 2006, **97**, 103001.
31 M. Cococcioni and S. de Gironcoli, *Phys. Rev. B: Condens. Matter Mater. Phys.*, 2005, **71**, 035105.
32 N. Marom, A. Tkatchenko, M. Rossi, V. V. Gobre, O. Hod, M. Scheffler and L. Kronik, *J. Chem. Theory Comput.*, 2011, **7**, 3944–3951.
33 G. Henkelman, B. P. Uberuaga and H. Jónsson, *J. Chem. Phys.*, 2000, **113**, 9901–9904.
34 D. Datta, J. Li and V. B. Shenoy, *ACS Appl. Mater. Interfaces*, 2014, **6**, 1788–1795.
35 I. A. Courtney, J. S. Tse, O. Mao, J. Hafner and J. R. Dahn, *Phys. Rev. B: Condens. Matter Mater. Phys.*, 1998, **58**, 15583–15588.
36 H. H. Huang, X. Fan, D. J. Singh and W. T. Zheng, *Nanoscale*, 2020, **12**, 1247–1268.
37 T. Jin, H. Li, K. Zhu, P. F. Wang, P. Liu and L. Jiao, *Chem. Soc. Rev.*, 2020, **49**, 2342–2377.
38 Y. Lyu, Y. Liu, Z.-E. Yu, N. Su, Y. Liu, W. Li, Q. Li, B. Guo and B. Liu, *Sustainable Mater. Technol.*, 2019, **21**, e00098.